



# Toward Multiscale Model Development for Multiphase Flow: Direct Numerical Simulation of Dispersed Phases and Multiscale Interfaces in a Gas-Stirred Ladle

QIANG LI <sup>1,3</sup> and PETRUS CHRISTIAAN PISTORIUS <sup>2</sup>

1.—School of Metallurgy, Northeastern University, Heping District, Shenyang 110819, China.  
2.—Department of Materials Science and Engineering, Carnegie Mellon University, Pittsburgh, PA 15213, USA. 3.—e-mail: liq@smm.neu.edu.cn

Insights into dispersed phases, such as bubbles and droplets, and multiscale interfaces in a gas-stirred ladle are of great significance to multiphase systems of metallurgical reactors, but are still challenging and not fully understood. A direct numerical simulation of dispersing phases was developed, coupling a sub-grid-scale large-eddy simulation for turbulence in fine grids with local refinement tactics. After validation with experimental data, the model was applied to investigate the bubble formation process at small length scales to understand the mechanism of bubble breakup and coalescence, to reveal the interaction of bubbles with surrounding fluid and the evolution of heterogeneous vortex structures, to compare transient phenomena and time-averaged behavior, and to resolve the large-scale interface profile and the large number of small droplets formed by the interaction of metal, slag, and gas. The availability of results from the bubble/droplet scale using the current simulations should help advance new closure relations for the average or large-scale flows toward a multiscale model.

## INTRODUCTION

Small-scale bubbles, droplets, and multiscale interfaces commonly coexist in many industrial engineering applications.<sup>1–3</sup> A typical example is in gas-stirred ladles,<sup>4</sup> which are widely employed in the modern steelmaking industry for refining and homogenization purposes. In ladle operations, inert argon or nitrogen gas injection from bottom plug(s) into the bath—containing liquid metal and slag—creates one or multiple bubble plume(s) and forms a bubble-driven flow field. Where the bubbles impinge on interfaces between liquids, many droplets form, with a wide range of sizes, and emulsification can occur.<sup>2,3,5,6</sup> The characteristics of these dispersing phases and multiscale interfaces play critical roles in mass, momentum, and energy transfer and thus affect the refining efficiency, unit performance, and final product quality. Nonetheless, to date, there have been few studies on

dispersed phases, such as distribution in the continuous phase, and dispersed phase generation, aggregation and fragmentation, and entrainment; studying these characteristics is challenging, particularly at a high temperature under hazardous conditions, because of the limits of measurement technology and the high costs of in situ experimentation.

Computational modeling has been widely used in predicting and investigating multiphase flow problems.<sup>7–11</sup> Several mature modeling methods have been developed to reproduce flow behavior and large-scale features.<sup>8–20</sup> Figure 1 shows a roadmap for the evolution of mathematical models and a conceptual illustration of simulation frameworks, including the Eulerian–Eulerian approach (E–E),<sup>12–19</sup> Eulerian–Lagrangian approach (E–L),<sup>20–28</sup> and dispersed phases resolved direct numerical simulation approach (DPR-DNS) developed by us.<sup>29</sup> The E–E and E–L methods are most commonly used to simulate two-phase and multiphase flows. For these two approaches, when the volume of fluid (VoF) method is used to track the large-scale

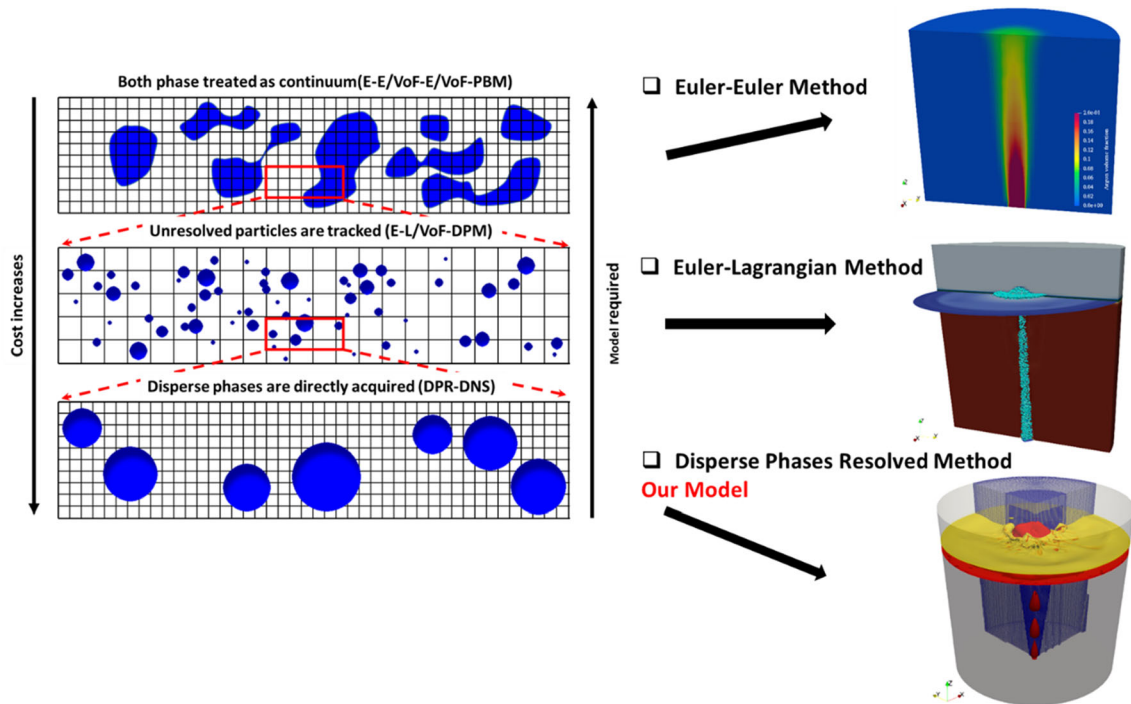


Fig. 1. Conceptual illustration of the simulation frameworks including E-E/VoF-E/VoF-PBM, E-L/VoF-DPM, and DPR-DNS method.

interface of continuous phase(s), the models also are termed the VoF-E and VoF-L methods, or VoF with discrete particle model (VoF-DMP). However, with the addition of the VoF method, the inherent way in which the dispersed phases are treated remains the same and requires a model to close the constitutive relation. As examples, Zhang and Taniguchi<sup>30</sup> and Li et al.<sup>13</sup> employed the VoF-E method to investigate large-scale slag layer behavior; Cao et al.<sup>31,32</sup> used a VoF-DPM model to study the transport and removal of inclusions and slag-metal reactions including desulfurization behavior; Cloete et al.<sup>33,34</sup>, Liu et al.<sup>35</sup>, Mantripragada and Sarkar,<sup>36</sup> and Ramasetti et al.<sup>37,38</sup> developed VoF-E models to track the large-scale interfaces and proposed regressions for the slag eye size; Zhu et al.<sup>39</sup> studied slag eye behavior using a VoF-E approach. These two methods have their advantages and limitations, which have been detailed in the literature.<sup>40</sup> Both approaches are often coupled with the population balance modeling (PBM) method,<sup>41,42</sup> which provides a way to consider the size distribution of bubbles and their interaction with each other, such as collision, coalescence, and breakup. For example, Li et al.<sup>27,28</sup> applied VoF-DPM and VoF-PBM models to consider the bubble size distribution and to model the bubble coalescence. Morales et al.<sup>41,42</sup> combined VoF-E with PBM to consider bubble breakup and aggregation, investigating the slag thickness effect and flow structure in a ladle. However, with this approach detailed information on bubble shape and deformation in plume flow is

not available, despite their importance to mixing and mass and heat transfer. For the models to close the drag and lift forces, model calibration and validation require extra effort.

An alternative approach—DPR-DNS—has been described in our recent work, which is based on the VoF type method to resolve the dispersed phase, applied to study slag eye behavior.<sup>29</sup> The key differentiating feature of DPR-DNS is its ability to directly simulate the dispersed phases and small-scale interfaces, with the capacity to reveal some important mechanisms and build a closure relation to the larger-scale models and simulations. It should be stressed that for the simulation frameworks shown in Fig. 1, when transitioning from E-E to E-L and further to DPR-DNS, more computational resources are required, but with less use of fitted models (constitutive relations), while allowing more phenomena and mechanisms to be solved directly. A hierarchical multiscale model would couple these approaches; this is the target of future work. Here, the focus is on modeling small-scale phenomena.

This article presents a direct numerical simulation study of bubbles, droplets, and multiscale interfaces. After the validation of the model, the formation, aggregation, and breakup of bubbles were visualized using VoF-based DPR-DNS simulation. In addition, the unsteady heterogeneous bubble flow structure was investigated at the mesoscale. Interaction between bubbles and the surrounding fluid was analyzed in detail, and a new aggregation mechanism of inclusions in the

turbulent vortex core is reported. The evolution of large-scale phase interface profiles was shown and the generation mechanism of droplets was revealed using this direct numerical simulation.

## MODEL FORMULATION

The DPR-DNS-VoF method has been reported in our recent study on slag eye behavior;<sup>29</sup> some improvements have been made for the present work; hence, the method is outlined as follows.

### DPR-DNS-VoF Methodology

Disperse-phases-resolved direct numerical simulation (DPR-DNS) is here based on the VoF<sup>43,44</sup> type method, termed as DPR-DNS-VoF. The main advantage of the DPR-DNS-VoF is to directly acquire the dispersed phases in a fine grid without employing any constitutive relations, while the traditional VoF with a relatively coarser grid compared to the scale of the dispersed phase is usually used to solve the large-scale free surface or interface(s) among phases. To simulate the multiphase system in a gas-stirred ladle, some assumptions were made as detailed in our previous work.<sup>29</sup> The hydrodynamics of this multiphase system is governed by a single set of Navier-Stokes equations and a continuity equation.

$$\frac{\partial \rho}{\partial t} + \frac{\partial(\rho u_i)}{\partial x_i} = 0 \quad (1)$$

$$\frac{\partial \rho u_i}{\partial t} + \frac{\partial(\rho u_i u_j)}{\partial x_j} = -\frac{\partial p}{\partial x_i} + \frac{\partial \tau_{ij}^{\text{sgs}}}{\partial x_j} + \rho g_i + f_\sigma \quad (2)$$

Here,  $u_i$  and  $u_j$  are the velocity components in the  $i$  and  $j$  directions ( $\text{m}\cdot\text{s}^{-1}$ );  $t$  is the time (s);  $p$  is the pressure (Pa);  $g$  is the gravity acceleration ( $\text{m}\cdot\text{s}^{-2}$ );  $\tau_{ij}^{\text{sgs}}$  is the sub-grid stress tensor ( $\text{N}\cdot\text{m}^{-2}$ ), which is calculated as follows:

$$\tau_{ij}^{\text{sgs}} = \mu_{\text{eff}} \left( \frac{\partial u_i}{\partial x_j} + \frac{\partial u_j}{\partial x_i} \right) - \frac{2}{3} \mu_{\text{eff}} \frac{\partial u_k}{\partial x_k} \delta_{ij} \quad (3)$$

where  $\delta_{ij}$  is the Kronecker delta ( $\delta_{ij} = 1$  if  $i = j$ , and  $\delta_{ij} = 0$  if  $i \neq j$ );  $\mu_{\text{eff}}$  is the effective viscosity ( $\text{Pa}\cdot\text{s}$ ) calculated by:

$$\mu_{\text{eff}} = \mu + \mu_t \quad (4)$$

where  $\mu$  is the molecular viscosity ( $\text{Pa}\cdot\text{s}$ ), and the turbulent viscosity  $\mu_t$  ( $\text{Pa}\cdot\text{s}$ ) is calculated by the turbulence model.

In the present study, a modified approach was used, based on the multi-fluid formulation proposed by Ubbink and Issa.<sup>45</sup> The evolution of an interface or free surface is described by an additional transport equation for the indicator function (representing the volume fraction of one phase) that needs to be solved together with the continuity and momentum equations:

$$\frac{\partial \alpha_q}{\partial t} + \frac{\partial(u_i \alpha_q)}{\partial x_i} + \frac{\partial(u_{i,r} \alpha_q (1 - \alpha_q))}{\partial x_i} = 0 \quad (5)$$

where  $u_{i,r} = u_{i,q} - u_{i,p}$  is the relative velocity ( $\text{m}\cdot\text{s}^{-1}$ ) between phase  $q$  and phase  $p$ . Here, the third term on the left hand of Eq. 5 is added to bring in a counter-gradient artificial interface compression term, in which  $u_{i,r}$  ensures compression with a suitable compression velocity, while the  $\partial/\partial x_i$  operation guarantees conservation and  $\alpha_q(1 - \alpha_q)$  guarantees boundedness with the compression acting only in the interface region.<sup>46</sup>

In each cell, the volume fractions of all phases sum to unity, i.e.,

$$\sum_{q=1}^n \alpha_q = 1 \quad (6)$$

The one-fluid formulation relies on the fact that multiple fluids (or phases) are not interpenetrating. Because the same immiscible fluids are considered an effective fluid throughout the domain, the momentum equations shared by all phases are solved with an effective density  $\rho$  ( $\text{kg}\cdot\text{m}^{-3}$ ) and an effective viscosity  $\mu$  ( $\text{Pa}\cdot\text{s}$ ). The fluid properties are calculated by a weighted averaging method based on the volume fraction of each phase. The volume-fraction-averaged density and viscosity are calculated, respectively, by:

$$\rho = \sum_q \alpha_q \rho_q \quad (7)$$

$$\mu = \sum_q \alpha_q \mu_q \quad (8)$$

In Eqs. (1)–(8), the subscript  $q$  denotes the metal, slag, and gas phases.

To consider the effect of surface tension, an additional term is included in the momentum equation as  $f_\sigma$  on the interface  $S(t)$ , calculated per unit volume using the continuum surface force model with the following expression:

$$f_\sigma = \sum_q \left( \int_{S(t)} \sigma_{q,p} \kappa_q \nabla \alpha_q dS \right) \quad (9)$$

where  $\sigma_{q,p}$  is the interfacial tension between phase  $q$  and phase  $p$  ( $\text{N}\cdot\text{m}^{-1}$ );  $\kappa_q$  is the mean curvature of the interface of phase  $q$ , which is determined by:

$$\kappa_q = -\nabla \cdot \left( \frac{\nabla \alpha_q}{|\nabla \alpha_q|} \right) \quad (10)$$

### One-Equation LES Model

In LES, the larger length scales are resolved directly and the smaller scales are described with a model. A low-pass filter is applied to separate the resolved and sub-grid scale. The set of Eqs. (1–4) was re-formulated (according to the LES decomposition) into resolved fields and sub-grid fields. The filtered equations have a fully similar form except for additional sub-grid scale (SGS) stress terms that

need to be closed, resulting from the filtering procedure. In the current study, the filter size  $\Delta$  and shape were fixed by the computational element size and shape; therefore, a box filter was adopted. The sub-grid scale (SGS) kinetic energy is defined as:

$$k_{\text{sgs}} = \frac{1}{2}(\overline{u_k u_k} - \overline{u_k} \overline{u_k}) \quad (11)$$

where the overbar ( $\overline{\quad}$ ) denotes the application of grid filter. Both the original and dynamic Smagorinsky models are essentially algebraic models.<sup>47</sup> The underlying assumption is that there is a local equilibrium between the transferred kinetic energy through the grid filter. The SGS turbulence is represented more faithfully by accounting for the transport of SGS kinetic energy; the approach can account for the history and non-local effects. Thus, the present study adopted the one-equation LES model,<sup>48,49</sup> and the transport equation for sub-grid scale kinetic energy is solved.

$$\frac{\partial k_{\text{sgs}}}{\partial t} + \frac{\partial \overline{u_j} k_{\text{sgs}}}{\partial x_j} = \frac{\partial}{\partial x_j} \left( \frac{\mu_t}{\sigma_k} \frac{\partial k_{\text{sgs}}}{\partial x_j} \right) - \tau_{ij} \frac{\partial \overline{u_j}}{\partial x_j} - C_\epsilon \frac{k_{\text{sgs}}^{3/2}}{\Delta} \quad (12)$$

where constants  $C_\epsilon$  and  $\sigma_k$  are taken as 0.916 and 1.0, respectively. The sub-grid scale stress can be expressed as:

$$\tau_{ij} = -2\mu_t S_{ij} + \frac{2}{3}k_{\text{sgs}}\delta_{ij} \quad (13)$$

The sub-grid eddy viscosity can be computed as:

$$\mu_t = C_k k_{\text{sgs}}^{1/2} \Delta \quad (14)$$

Here,  $S_{ij} = \frac{1}{2}(\frac{\partial u_i}{\partial x_j} + \frac{\partial u_j}{\partial x_i})$  is the rate of deformation tensor and  $C_k$  is taken as 0.09.

## Computational Details

The simulation target is a 150-ton industrial gas-stirred ladle. The geometrical parameters, operational conditions, and physical properties of fluids in this study are the same as those used by our recent study,<sup>29</sup> apart from the gas flow rates considered in the present numerical experiments, which are 1000 L/min and 2000 L/min. Note that our computational parameters are based on a steelmaking temperature of 1600 °C and ambient pressure.

The grid resolution is remarkably important to the DPR-DNS-VoF method and for LES simulation. This study used a block-structured curvilinear O-ring type mesh, which consisted of a central square block of  $160 \times 160$  elements surrounded by four blocks with  $40 \times 160$  elements in the radial direction. Figure 2a gives the computational domain and typical mesh configuration. An important characteristic of this design is that it guarantees that the region of interest has a high-quality fully orthogonal Cartesian mesh with a uniform distribution of cubic hexahedral grids. Additionally, local refinement has been applied, with the approach shown in Fig. 2b and c. Previous work showed that

the flow pattern in a gas-stirred ladle is dominated by the bubble plume;<sup>29</sup> this was the basis for restricting the refined region to an inverted-cone shape, shown in the central zone of Fig. 2a and b. Figure 2c further illustrates the effect of grid refinement on the ability to resolve small-scale interfaces. When the grid is refined once, the length of the dispersed phases that can be resolved is 1/2 of the original (1/8 of the volume). With two grid refinements, the minimum resolved volume of the dispersed phase is reduced to 1/64 of the original. Furthermore, the adaptive mesh refinement (AMR)<sup>50</sup> based on the octrees spatial discretization technology with dynamic loading balance (DLB)<sup>51</sup> is a key feature of the code implementation of our model, which enables ready acquisition of the characteristic target dimension for dispersed phases based on the local refinement tactics, with the code run in parallel at near capacity on a cluster. To correctly resolve the dispersed phases such as the bubbles and droplets, the refinement process is automatically triggered around the phase interfaces following the user-defined criteria. The refinement is performed to be at the maximum level, which is fixed at 3, around the phase interface based on the criterion of phase fraction  $< 0.2$  in this study. Otherwise, when regions that had contained interfaces become a single-phase region with the evolution of computational time, the mesh is allowed to de-refine to save simulation resources.

In the present study, the time step was self-adapting, with modifications based on the global and interface Courant numbers (CoN); for all simulations both CoNs were set to  $< 0.2$ . The simulations were performed on a CPU+GPU hybrid cluster with 9 nodes and a total of 108 cores. Any node is composed of two sockets, each containing a 2.67 GHz Intel Sandy Bridge with 12 Intel Xeon X5650 CPU cores. Each core offers 64 GB of memory. The nodes are interconnected by an InfiniBand QDR Network. When a case runs, the meshes are decomposed using a simple geometric decomposition algorithm in which the domain is split into pieces by direction based on the number of parallel cores. The run time of one typical case was about 2 weeks.

## RESULTS AND DISCUSSION

### Model Validation

Model validation has been reported in our previous study,<sup>29</sup> comparing model results with experiments and theoretical equations. Here, a side-by-side comparison of the flow pattern in our numerical simulation result (see Fig. 3a) and a water model<sup>52</sup> (see Fig. 3b) is shown. It can be observed that the dispersion pattern of injected gas has been directly captured and reasonable agreement between the predicted and experimental results achieved. Also, this typical snapshot indicates that the plume is a heterogeneous structure, with small-scale bubbles traveling upwards chaotically, while expanding

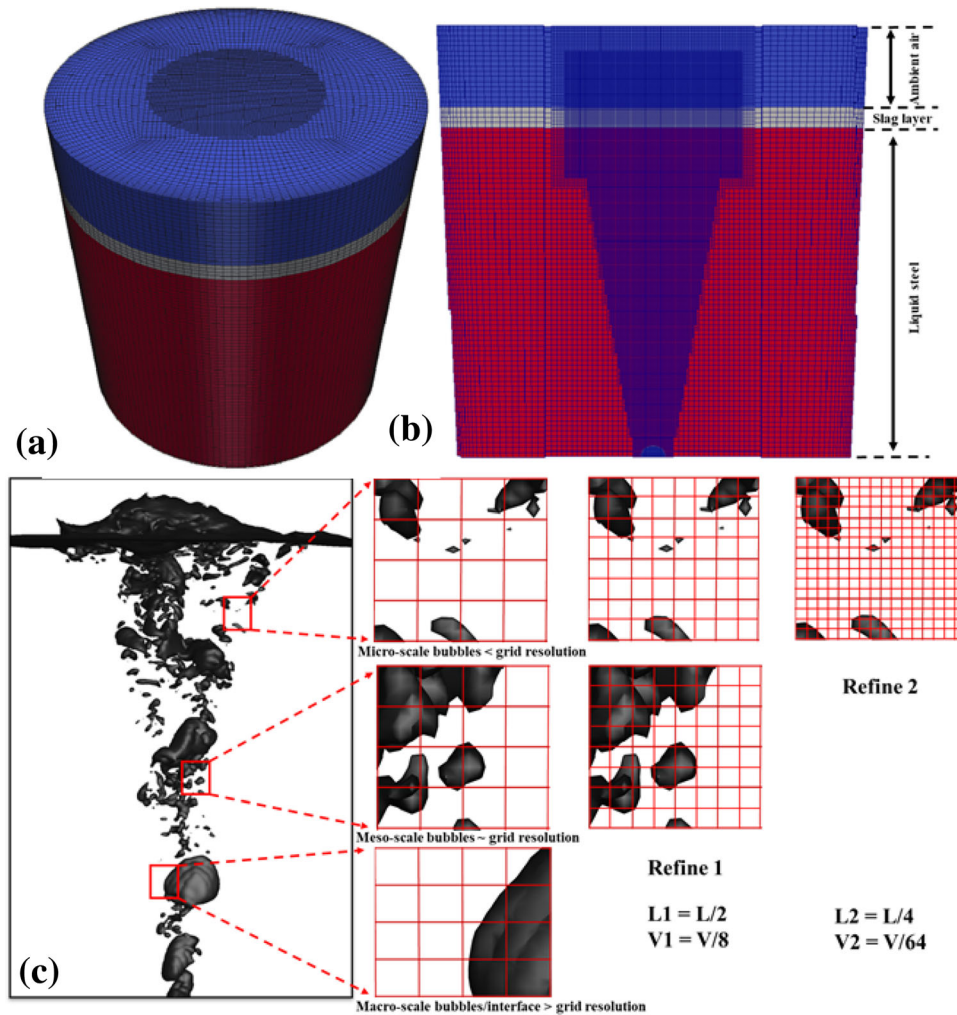


Fig. 2. Illustration of computational detail: (a) the computational domain and (b) corresponding meshing strategy to accurately acquire the small-scale phenomena; (c) the mesh refinement, and the capacity to capture dispersed phases, was doubled in each step.

radially to create the two-phase plume region; where the gas escapes from the liquid surface an emulsification region is formed. These phenomena and bubble structures are directly revealed by the present model, but would be difficult to capture by traditional large-scale CFD/VoF methods without the local refine tactics of dynamic AMR coupled with DLB.

### Bubble Formation, Breakup, and Coalescence

Figure 4 shows snapshots of rising bubbles captured by DPR-DNS-VoF at consecutive time steps ( $\Delta t = 50$  ms) at a gas flow rate of 1000 L/min; other conditions can be found in our recent work.<sup>29</sup> Figure 4a shows the formation of the first bubble in a quiescent bath; the evolution of the bubble shape is shown, as the kinetic energy of the injected gas is converted to overcome the bath pressure and surface tension. As the bubble grows, the buoyancy force arising from the density difference between the phases increases, and at some instant—0.35s for this case—the necking stage is reached: the bubble

neck shrinks to zero; the bubble detaches from the inlet surface and moves toward the fluid bulk, forming a free bubble. This case was for the first bubble formed at the start of gas injection; for fully developed stirring, additional phenomena are observed: bubble detachment is also affected by the shear stress due to the oscillating flow field perpendicular to the bubble rising direction. The result is that the frequency of bubble detachment is higher and the bubble is deformed more compared with the first one; see Fig. 4b and c. The simulations also showed that, when a bubble detaches from the inlet, a low-pressure region between this bubble and the inlet (caused by the bubble wake) promotes agglomeration of this bubble and the next to form.

After bubbles form, as their flotation velocity increases, one might expect a balance between the drag force and the buoyant force. However, the bubbles deform under the influence of the applied forces, changing shape to reduce the drag force, or coalescence can occur (induced by the wake of preceding bubbles), or bubbles can disintegrate into

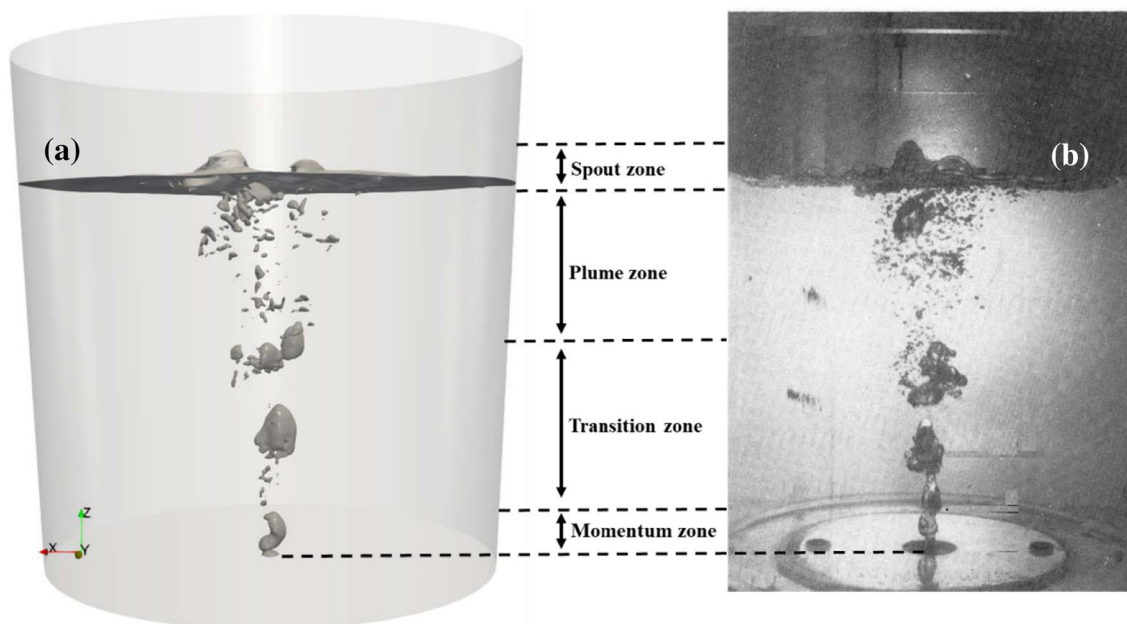


Fig. 3. A comparison of heterogeneous structure of bubbles flow between (a) our numerical results and (b) experimental results.

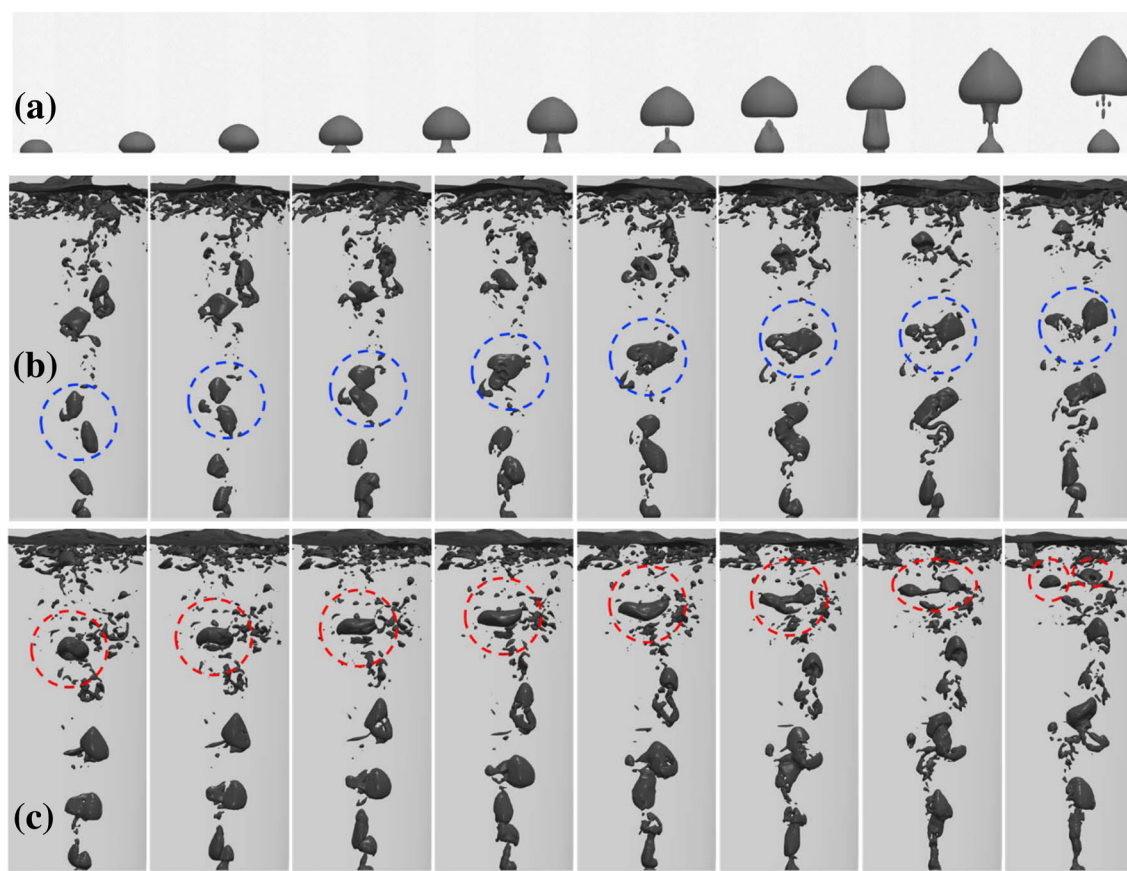


Fig. 4. Instantaneous snapshots of rising bubbles captured by DPR-DNS-VoF at consecutive time steps ( $\Delta t = 50$  ms); gas flow rate 1000 L/min, showing the following phenomena: (a) formation of the first bubble in a quiescent bath; (b) bubble aggregation; (c) bubble deformation and disintegration.

small bubbles with a range of sizes. Figure 4b and c shows examples of bubble deformation, coalescence, and disintegrating found with the present model; collision and aggregation are highlighted using blue circles. The example in Fig. 4b shows disintegration after the merging of two bubbles. The coalescence of bubbles occurs by the wake effect, forming a negative pressure that attracts the following bubble to contact the preceding bubble, thus inducing aggregation. Figure 4c shows an example of bubble deformation and disintegration directly captured by this simulation (highlighted by the red dashed circles). In the early stage the bubble undergoes a series of successive small deformations, then the bubble is stretched crosswise, and a large distortion leads to the final disintegration of the bubble and its separation into small bubbles. Unlike traditional CFD models, DPR-DNS-VoF can directly capture the mesoscale bubble structure and their time evolution without requiring any closure relation to model the bubble shape, deformation, disintegration, and coalescence behavior.

## Heterogeneous Vortex Structures

Ladle mixing and mass transfer are strongly influenced by the plume(s) flow structure. Figure 5 shows the evolution of bubble flow patterns (see Fig. 5a) and the turbulent vortex structures induced by these bubbles. Bubble shapes are depicted based on the iso-surfaces with volume fraction  $\alpha = 0.5$ . Vortices are identified by using the  $Q$  criterion, here using  $Q = 50$ ; see Fig. 5b. The  $Q$  criterion identifies structures with coherent fluid flow characteristics and helps to distinguish between the vortex zone and the shear motion zone. Vortices are defined as regions where the vorticity magnitude is greater than the magnitude of rate of strain, i.e.,  $Q = \frac{1}{2}(\Omega^2 - S^2)$ , where  $S$  is the shear strain rate and  $\Omega$  the vorticity magnitude.

Figure 5b and c shows that vorticity shed from the interface of large bubbles created many hairpin vortices. The spatially coherent, temporally evolving motions of hairpin vortices dominate the plume zone. The cores of the vortices likely provide favorable regions for the collision and aggregation of inclusions due to the local centrifugal motion caused by the density difference between inclusions and the

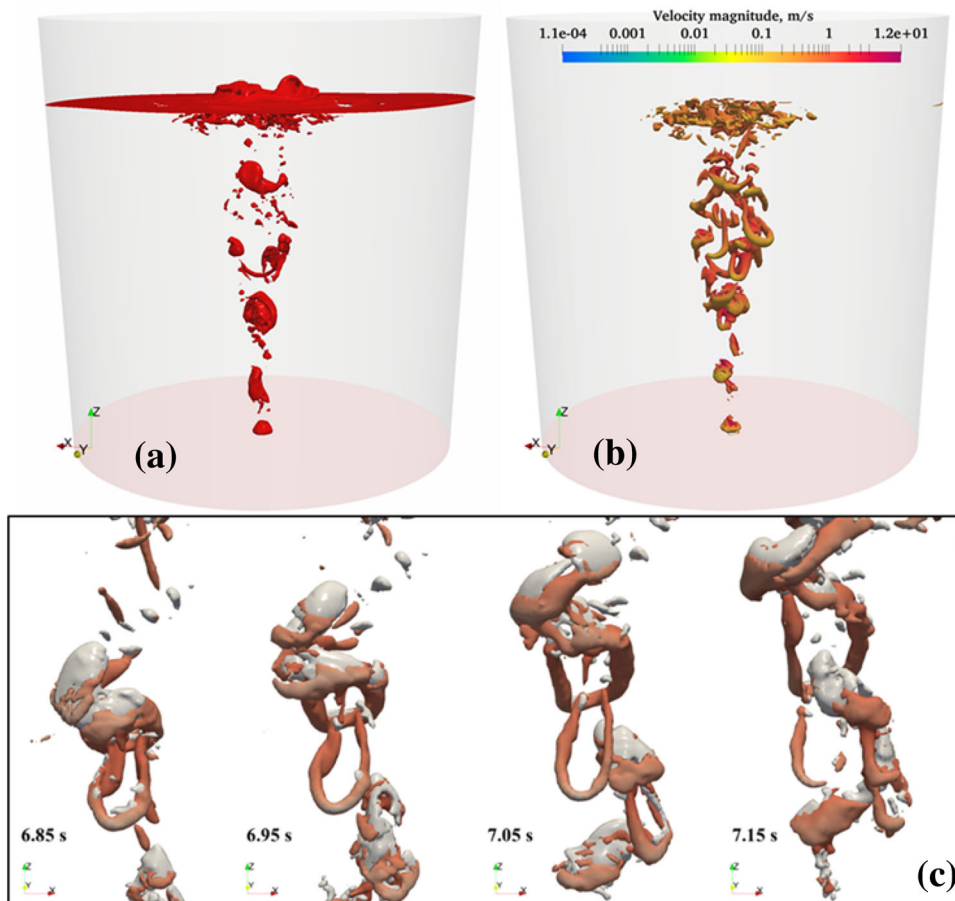


Fig. 5. Bubble plume hydrodynamics, showing (a) interaction of bubbles and surrounding fluid phase, (b) vortex structure induced by the bubbles, visualized with a  $Q$ -criterion of 50, and (c) close-up views of the evolution of the vortex structure.

liquid metal. Agglomeration in hairpin vortices may be a significant contributor to inclusion removal, in addition to those mechanisms previously suggested. The existing proposed mechanisms of inclusion removal rely on bubble attachment and the bubble wake effect. This work suggests that small inclusions may be trapped readily inside a hairpin core, grow by agglomeration, and be removed by floating from the steel. It should be stressed that this proposed mechanism only comes from the findings of our mesoscale simulation and has not yet been experimentally proven. On the other hand, bubble momentum is also transported into the liquid bath by these vortices, providing a means of producing turbulent kinetic energy. As the flow develops further, the turbulence is dissipated rapidly into the recirculation flow.

The plume consists of heterogeneous bubbles and vortices. Figure 5c gives a close-up view of the evolution of the vortex structure: the formation and shedding of hairpin vortices from bubbles can be seen. (In this figure, the light gray areas are the

bubbles and colored regions are vortex structures defined by iso-surfaces with a  $Q$ -criterion of 100.)

### Transient Versus Time-Averaged Behavior

Figure 6a shows the evolution of bubble plume structures at time intervals of 2.5 s; (b) shows the time-averaged plume profile over 30 s. The figures emphasize that the transient behavior occurs even under nominally steady-state conditions. In the left part of Fig. 6a, a typical transient snapshot of the entire ladle is shown, including streamlines in the molten steel, the interfaces between phases, and spout region; the right-hand part of this figure shows the transient bubble flow structures of plumes at different instants. It can be observed that the bubble swarms oscillate transversely, and the shape and flow behavior of the bubble plume are unsteady, heterogeneous, and change over time. These changes are likely to affect fluid flow, mass transfer, and inclusion removal. Bubble plume oscillation has been addressed in few previous studies (due to the limits of the numerical models), but some

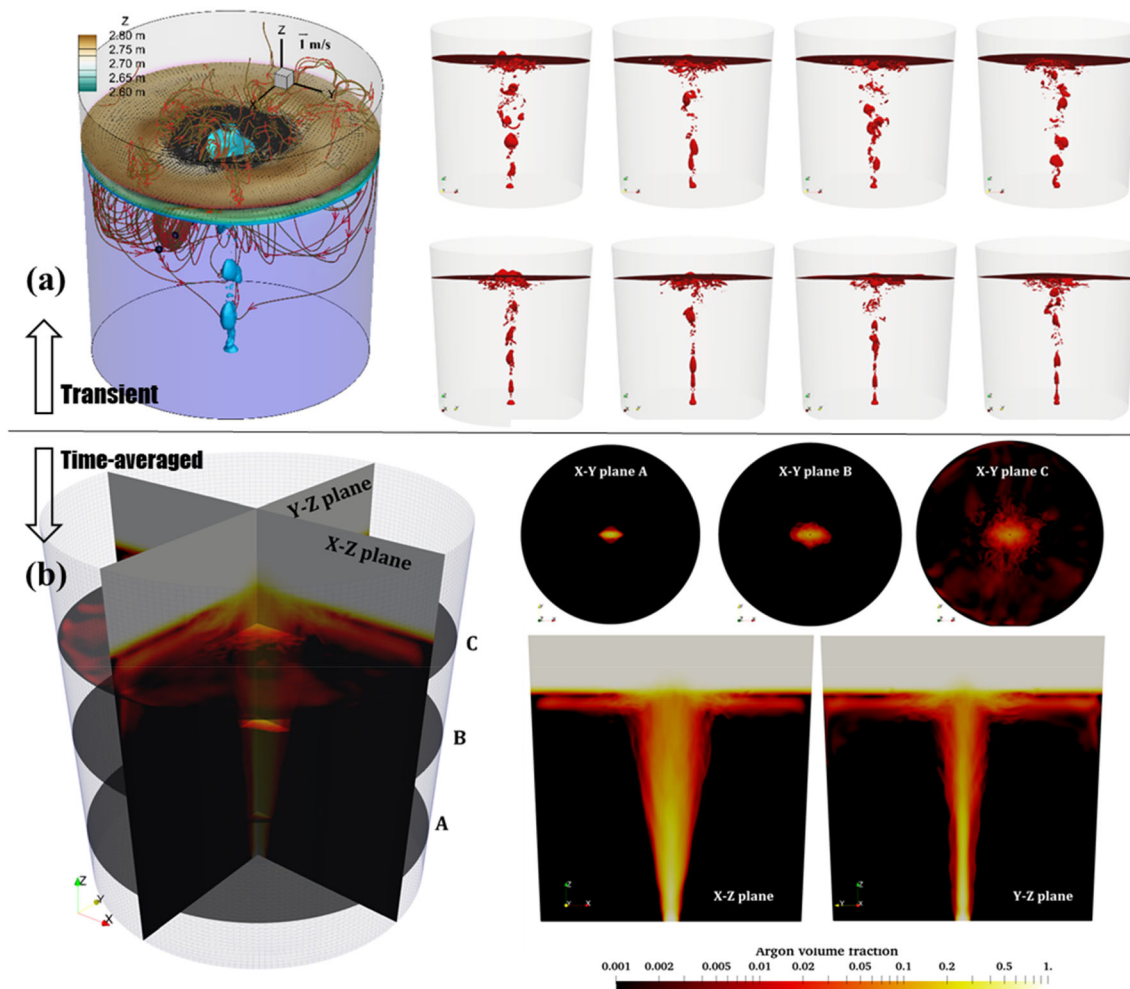


Fig. 6. Comparison of transient versus time-averaged phenomena: (a) typical transient snapshot of the entire ladle and the evolution history of transient bubble flow structures of plumes. (b) Time-averaged result with details shown on  $x$ - $y$  planes A, B, and C, and the  $x$ - $z$  and  $y$ - $z$  planes, of argon volume fraction.



experimental observations of this phenomenon have been reported.<sup>53</sup> The unsteady oscillation of bubble plumes is essentially attributed to the paths followed by rising free bubbles and bubble shape instability. The time-averaged plume is shown in Fig. 6b. Interestingly, for the time period considered (30 s), the bubble paths demonstrate a predominate

direction: the plume is a flattened cone instead of a regular cone.

### Large-Scale Interface Morphology and Small-Scale Droplets

In addition to small-scale bubble behavior, the simulation also reveals the large-scale interface morphology and slag eye evolution. Some results have

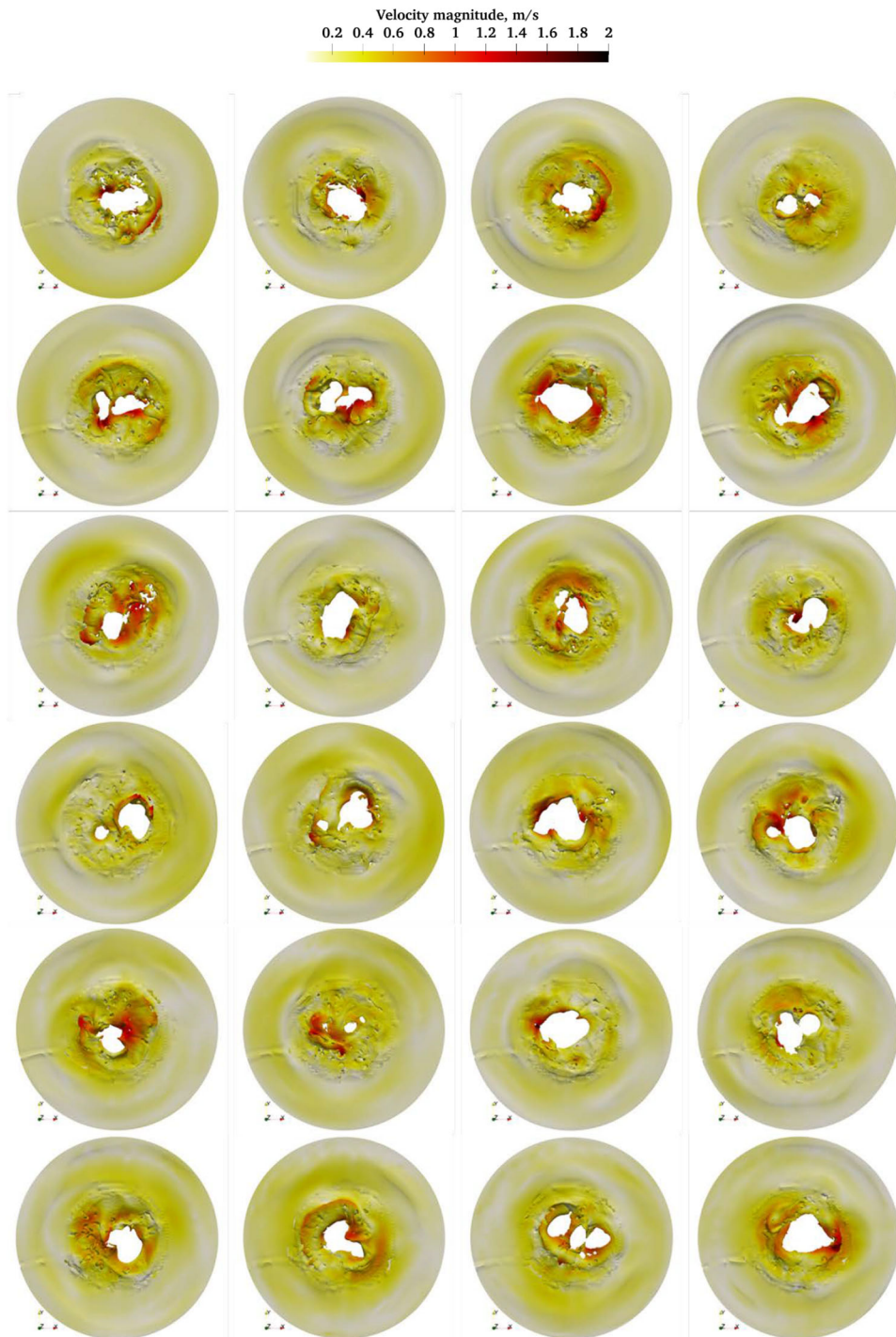


Fig. 7. Series of consecutive snapshots illustrating the dynamic behavior of the slag layer and open spout region. The time lapse between consecutive snapshots is 0.5 s; the images are ordered from left to right and from top to bottom.

been reported in our previous work;<sup>29</sup> some further examples are given in this section. Figure 7 shows a series of snapshots (at 0.5-s intervals) to illustrate the dynamic behavior of the slag layer and open eye region (gas flow rate of 1000 L/min). The top view is shown, visualizing only molten slag. The figure emphasizes that the shape of the slag eye changes continuously and dynamically. The color contours in Fig. 7 depict the distribution of velocity on the upper surface of the

slag layer; the velocity around the rim of the slag eye is usually relatively large because of interaction between the rising bubble plume and slag-metal interface. This zone is likely a region where slag becomes entrapped in the metal.

Figure 8 further shows slag droplet generation and fluctuation over time. Many slag droplets (with different sizes) are created at the slag eye rim. In Fig. 8, the view is radially from the center of the

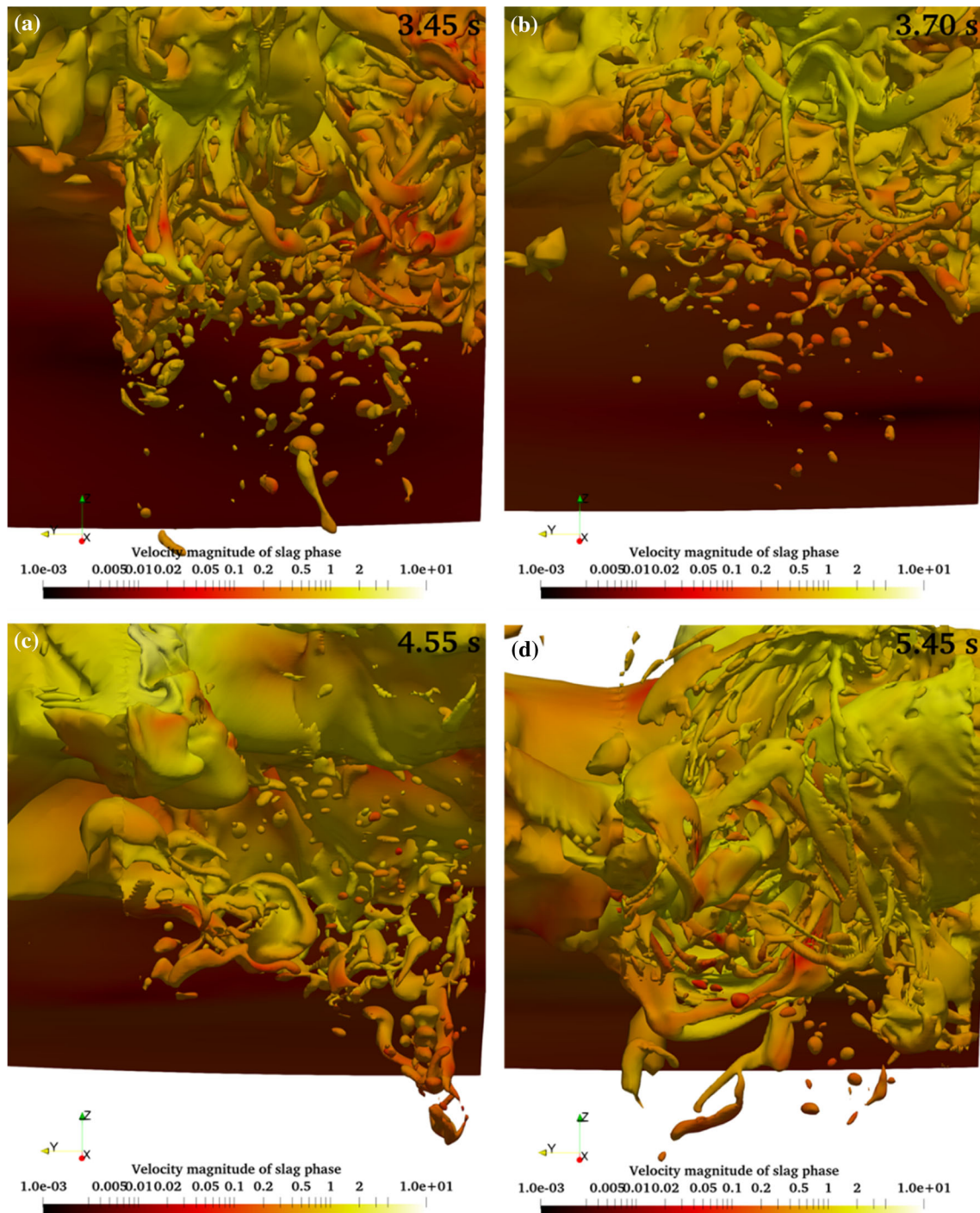


Fig. 8. Droplet generation process and fluctuations with time: (a) 3.45 s, (b) 3.70 s, (c) 4.55 s, and (d) 5.45 s.

vessel to the edge of the slag eye. Fluctuation of the number of droplets with time depends on the intensity and frequency of metal and slag interaction. When the shear force at the slag-steel interface—induced by the motion of the metal falling back from the spout into the bulk—is sufficiently large, it breaks up the slag phase, forming the ligaments or droplets. The frequency and size of bubbles impinging on the region directly influence this interaction.

Finally, it should be emphasized that the present study represents our initial efforts toward a full understanding of small-scale phenomena of dispersed phases and establishing a multiscale closure relation for a macro-scale model or time-averaged model of an industrial scale multiphase reactor. The present research framework appears promising, but further model development and investigations are needed. Future research targets include quantifying the size and number distribution of droplets and determining the mass transfer coefficient of refining reactions.

## CONCLUSION

The dispersing phases—gas bubbles and slag droplets—and interface profiles were investigated and directly visualized by the DPR-DNS-VoF method. Some interesting phenomena found in the present study are summarized as follows:

1. In model validation, the heterogeneous structure of a plume at bubble scale agreed with experiments.
2. The suction of negative pressure induced by the wake of preceding bubbles is a key cause of bubble aggregation. Direct simulation of dispersing phases clearly shows the detailed process of bubble formation, break-up, and coalescence.
3. The interaction between rising bubbles and the surrounding fluid creates many inherent hair-pin vortices; the vortex cores likely promote the collision and aggregation to inclusions.
4. The morphology of the open eye—formed by the escape from and impingement of bubbles on the slag layer—changes continuously and dynamically. The velocity around the rim of the slag eye is usually relatively large; the velocity gradient at the slag-metal interface breaks the slag bulk into sheets, ligaments, and droplets.

## ACKNOWLEDGEMENTS

Qiang Li acknowledges the financial support from the National Natural Science Foundation of China under Grant No. 52074079, the Fundamental Research Funds of the Central Universities of China under Grant No. N2125018, and the China Scholarship Council (No. 201706085028) as a visiting scholar in Carnegie Mellon University, USA.

## CONFLICT OF INTEREST

Additionally, on behalf of all authors, the corresponding author states no conflict of interest.

## REFERENCES

1. C.T. Crowe, J.D. Schwarzkopf, M. Sommerfeld and Y. Tsuji, *Multiphase Flows with Droplets and Particles* (CRC Press, Boca Raton, 2012), pp 4–20.
2. M.A. Rhamdhani, K.S. Coley and G.A. Brooks, *Metall. Mater. Trans. B* 36, 591. (2005).
3. M.A. Rhamdhani, G.A. Brooks and K.S. Coley, *Metall. Mater. Trans. B* 37, 1087. (2006).
4. D. Mazumdar and J.W. Evans, *Modelling of Steelmaking Process* (CRC Press, Boca Raton, 2009), pp 12–60.
5. N. Dogan, G. Brooks and M.A. Rhamdhani, *ISIJ Inter.* 49, 24. (2009).
6. M.A. Rhamdhani, K.S. Coley and G.A. Brooks, *Metall. Mater. Trans. B* 36, 219. (2005).
7. J.E. Olsen and Q.G. Reynolds, *Metall. Mater. Trans. B* 51, 1750. (2020).
8. M.M. Li, Q. Li, S.B. Kuang and Z.S. Zou, *Ind. Eng. Chem. Res.* 55, 3630 (2016).
9. Q. Li, M.M. Li, S.B. Kuang and Z.S. Zou, *Metall. Mater. Trans. B* 46, 1494. (2015).
10. Q. Li, M.M. Li, S.B. Kuang and Z.S. Zou, *JOM* 68, 3126. (2018).
11. M.M. Li, Q. Li, Z.S. Zou and B.K. Li, *JOM* 71, 729. (2019).
12. G. Venturini and M. Goldschmit, *Metall. Mater. Trans. B* 38, 461. (2007).
13. B.K. Li, H.B. Yin, C.Q. Zhou and F. Tsukihashi, *ISIJ Int.* 48, 1704. (2008).
14. F.P. Maldonado, M.A. Ramirez, A. Conejo and C. Gonzalez, *ISIJ Int.* 51, 1110. (2011).
15. W.T. Lou and M. Zhu, *Metall. Mater. Trans. B* 44, 1251. (2013).
16. W.T. Lou and M. Zhu, *Metall. Mater. Trans. B* 54, 9. (2014).
17. V. De Felice, I.L.A. Daoud, B. Dussoubs, A. Jardy and J.P. Bellot, *ISIJ Int.* 52, 1273. (2012).
18. J.P. Bellot, V. De Felice, B. Dussoubs, A. Jardy and S. Hans, *Metall. Mater. Trans. B* 45, 13. (2014).
19. L. Jonsson and P. Jönsson, *ISIJ Int.* 36, 1127. (1996).
20. L.M. Li, Z.Q. Liu, B.K. Li, H. Matsuura and F. Tsukihashi, *ISIJ Int.* 55, 1337. (2015).
21. L. Jonsson, D. Sichen and P. Jönsson, *ISIJ Int.* 38, 260. (1998).
22. Y. Sheng and G.A. Irons, *Metall. Mater. Trans. B* 24, 695. (1993).
23. D. Mazumdar and R.I.L. Guthrie, *ISIJ Int.* 34, 384. (1994).
24. H.P. Liu, Z.Y. Qi and M.G. Xu, *Steel Res. Int.* 82, 440. (2011).
25. Q. Cao and L. Nastac, *Metall. Mater. Trans. B* 49, 1388. (2018).
26. R. Singh, D. Mazumdar and A.K. Ray, *ISIJ Int.* 48, 1033. (2008).
27. L.M. Li, Z.Q. Liu, M.X. Cao and B.K. Li, *JOM* 67, 1459. (2015).
28. L.M. Li, B.K. Li and Z.Q. Liu, *ISIJ Int.* 57, 1. (2017).
29. Q. Li and P.C. Pistorius, *Metall. Mater. Trans. B.* <https://doi.org/10.1007/s11663-021-02121-w> (2021).
30. L.F. Zhang and S. Taniguchi, *Int. Mater. Rev.* 45, 59. (2000).
31. Q. Cao and L. Nastac, *Ironmaking Steelmaking* 45, 984. (2018).
32. Q. Cao, A. Pitts and L. Nastac, *Ironmaking Steelmaking* 45, 280. (2018).
33. S. Cloete, J.E. Olsen and P. Skjetne, *Appl. Ocean Res.* 31, 220. (2009).
34. S. Cloete, J.J. Eksteen and S.M. Bradshaw, *Mineral Eng.* 46, 16. (2013).
35. Y. Liu, M. Ersson, H.P. Liu, P. Jonsson and Y. Gan, *Steel Res. Int.* 90, 1. (2019).
36. V.T. Mantripragada and S. Sarkar, *Canadian Metal. Quart.* 59, 159. (2020).

37. E.K. Ramasetti, V.V. Visuri, P. Sulasalmi, R. Mattila and T. Fabritius, *Steel Res. Int.* 90, 1800365. (2019).
38. E.K. Ramasetti, V.V. Visuri, P. Sulasalmi, T. Palovaara, A.K. Kumar Gupta and T. Fabritius, *Steel Res. Int.*, 90, 1900088 (2019).
39. B.H. Zhu, B. Zhang and K. Chattopadhyay, *Metall. Trans. B* 51, 898. (2020).
40. Y. Liu, M. Ersson, H. Liu, P.G. Jonsson and Y. Gan, *Metall. Trans. B* 50, 555. (2019).
41. R.D. Morales, F.A. Calderón-Hurtado and K. Chattopadhyay, *Metall. Trans. B* 51, 628. (2020).
42. R.D. Morales, F.A. Calderón-Hurtado and K. Chattopadhyay, *ISIJ Inter.* 59, 1224. (2019).
43. C.W. Hirt and B.D. Nichols, *J. Comp. Phys.* 39, 201. (1981).
44. J.U. Brackbill, D.B. Kothe and C. Zemach, *J. Comp. Phys.* 100, 335. (1992).
45. O. Ubbink and R.I. Issa, *J. Comp. Phys.* 153, 26. (1999).
46. Rusche, H. Computational Fluid Dynamics of Dispersed Two-Phase Flows at High Phase Fractions. (Ph.D. Thesis, Imperial College London, London, UK, 2002), pp. 115-120.
47. J. Smagorinsky, *Month. Weather Rev.* 91, 99. (1963).
48. M. Germano, U. Piomelli, P. Moin and W.H. Cabot, *Phys. Fluids* 3, 1760. (1991).
49. B. Niceno, M.T. Dhotre and N.G. Deen, *Chem. Eng. Journal* 63, 3923. (2008).
50. G. Agbaglah, S. Delaux, D. Fuster, J. Hoepffner, C. Josseland, S. Popinet, P. Raya, R. Scardovelli and S. Zaleski, *C.R. Mec.* 339, 194. (2011).
51. N. Ahmad, M.N. Farooqi and D. Unat, *Sci. Program.* 2018, 1. (2018).
52. P.E. Anagbo, J.K. Brimacombe and A.H. Castillejos, *Canadian Metal. Quart.* 28, 323. (1989).
53. D. Laupsien, A. Cockx and A. Line, *Chem. Eng. Tech.* 40, 1484. (2017).

**Publisher's Note** Springer Nature remains neutral with regard to jurisdictional claims in published maps and institutional affiliations.